

Review

Novel Ultra-Sensitive Detectors in the 10–50 μm Wavelength Range

Takeji Ueda ^{1,2,*} and Susumu Komiyama ²

¹ CREST, Japan Science and Technology Agency/5 Sambancho, Chiyoda-ku, Yokyo, 102-0075, Japan

² Department of Basic Science, the University of Tokyo/3-8-1 Komaba, Meguro-ku, Tokyo, 153-8902, Japan; E-Mail: skomiyama@thz.c.u-tokyo.ac.jp

* Author to whom correspondence should be addressed; E-Mail: ueda@iis.u-tokyo.ac.jp; Tel.: +81-3-5454-6960; Fax: +81-3-5454-6960.

Received: 29 July 2010; in revised form: 13 August 2010 / Accepted: 31 August 2010 /

Published: 8 September 2010

Abstract: We have developed novel single-photon detectors in the 10–50 μm wavelength region. The detectors are charge-sensitive infrared phototransistors (CSIPs) fabricated in GaAs/AlGaAs double quantum well (QW) structures, in which a photo-generated hole (+e) in the floating gate (upper QW) modulates the conductance of a capacitively-coupled channel located underneath (lower QW). The excellent noise equivalent power ($NEP = 8.3 \times 10^{-19} \text{ W/Hz}^{1/2}$) and specific detectivity ($D^* = 8 \times 10^{14} \text{ cm Hz}^{1/2}/\text{W}$) are demonstrated for 15 micron detection up to 23 K, which are by a few orders of magnitude better than those of other state-of-the-art high-sensitivity detectors. The dynamic range exceeds 10^6 (~aW to pW) by repeatedly resetting the accumulated holes in the upper QW. Simple device structure makes the detectors feasible for array fabrication: Furthermore, monolithic integration with reading circuits will be possible.

Keywords: terahertz detector; far-infrared detector; ultra-sensitive detector; photon-counter; single-photon detector; charge-sensitive infrared phototransistor (CSIP)

1. Introduction

Terahertz (THz, ranging 0.3 THz–3 THz in frequency, or 100 μm –1 mm in wavelength) and far infrared (FIR, ranging 20 THz–430 THz, or 15 μm –300 μm) have become intensive, interdisciplinary

research fields in recent years [1-3], through long-term fundamental research and application development ground work. Historically, the THz-IR radiation has been researched and applied for heating technology and spectroscopy, but recent research and development are motivated by biology [4], astronomy [5], medicine [6], tele-communication [7], and security [8].

From the viewpoint of spectroscopy, the most remarkable feature of the FIR-THz range is the rich spectra of matter. This makes possible identification of solids, molecules and chemical bonds through *fingerprint*-like spectra. Another important feature is that the FIR-THz radiation is thermally emitted by every material at room temperature [1]. This makes FIR-THz radiation a unique tool for studying the temperature distribution and internal activity of materials. Because of this feature, highly-sensitive detectors have been in demand as the key technology in astrophysics [5]. Recent new technologies also require ultrasensitive detectors: high-resolution passive microscopy [9-11], as well as on-chip devices [12], in which single THz photons are generated, propagated and counted.

Differently from routinely used photon-counters in near-infrared or visible range, photon energies are far smaller ($h\nu < 124 \text{ meV}$ for $\lambda > 10 \text{ }\mu\text{m}$) and the single-photon detection is no longer trivial. In the last decade, a variety of novel detection schemes has been proposed [13-19]. Among them, only semiconductor quantum devices have demonstrated to produce clear single-photon signal against incident FIR-THz photons [14-17]. Charge-sensitive detector (CSIP) [17] is one of those semiconductor devices with single-photon sensitivity, but is far more useful than other ultrasensitive devices from various viewpoints: easy to use, high-speed, wide dynamic range, operable without dilution refrigerator, suitable to make large-array by simple planer structure. In this article the fundamental mechanism of CSIP as well as important experimental results are reviewed.

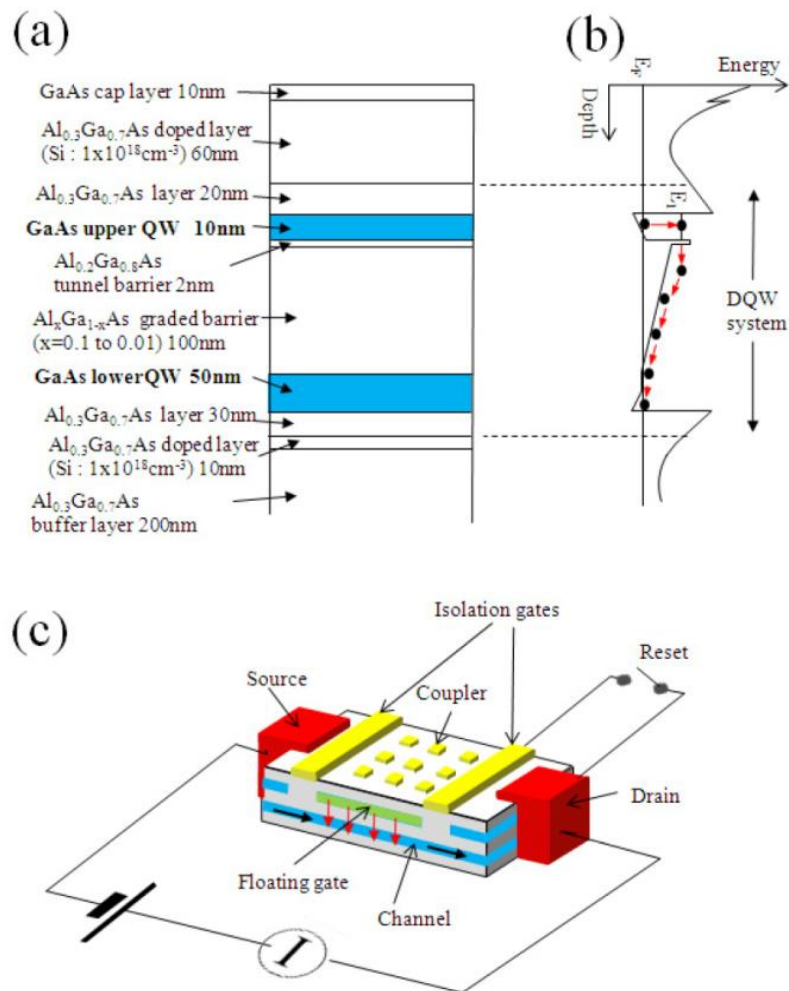
2. Device Structure and Detection Scheme

The detectors utilize a double-quantum well (DQW) structure (Figure 1(a)), where photo-excited electrons are generated via intersubband transition in the upper quantum well (QW). A photo-excited electron escapes out of the upper QW through the tunnel-barrier, and relaxes into the lower QW as shown in Figure 1(b). Since the upper QW is electrically isolated from the lower QW by negatively biasing the surface metal gates, the isolated upper QW is positively charged up due to the photo-excitation. The pile-up positive charge (hereafter referred to as a “photohole”) in the isolated upper QW is sensitively detected by an increase in conductance through the lower QW as shown in Figure 1(c). In short, the device works as a photo-sensitive field effective transistor with a photo-active floating gate served by the upper QW.

The epitaxial layers are grown by molecular-beam epitaxy on semi-insulating GaAs substrate [17,20-26]: They consist of a 1 μm thick buffer layer ($\text{Al}_{0.3}\text{Ga}_{0.7}\text{As}$ 20 nm/GaAs 2 nm superlattices), a Si doped ($1 \times 10^{18} \text{ cm}^{-3}$) 10 nm $\text{Al}_{0.3}\text{Ga}_{0.7}\text{As}$ electron-supply layer, a 30 nm $\text{Al}_{0.3}\text{Ga}_{0.7}\text{As}$ spacer layer, a 50 nm GaAs lower QW layer, a 100 nm composition graded $\text{Al}_x\text{Ga}_{1-x}\text{As}$ ($x = 0.01 \rightarrow 0.1$) barrier layer, a 2 nm $\text{Al}_{0.2}\text{Ga}_{0.8}\text{As}$ tunnel barrier, a 10 nm GaAs upper QW layer, a 20 nm $\text{Al}_{0.3}\text{Ga}_{0.7}\text{As}$ spacer layer, a Si doped ($1 \times 10^{18} \text{ cm}^{-3}$) 60 nm $\text{Al}_{0.3}\text{Ga}_{0.7}\text{As}$ layer, and a 10 nm GaAs cap layer. Typical electron density, N_s , and mobility, μ , are around $N_s = 3 \times 10^{11} \text{ cm}^{-2}$ and $\mu = 3 \times 10^4 \text{ cm}^2/\text{Vs}$ (for undoped QWs) or $100 \text{ cm}^2/\text{Vs}$ (for doped QWs), respectively. The above mentioned structure is for detecting $\lambda = 15 \text{ }\mu\text{m}$. For different wavelengths, the width of the upper QW

and height of the wall (confining barrier) as well as Si doping density inside QW are tuned so that intersubband transition energy correspond to the target wavelength [27,28].

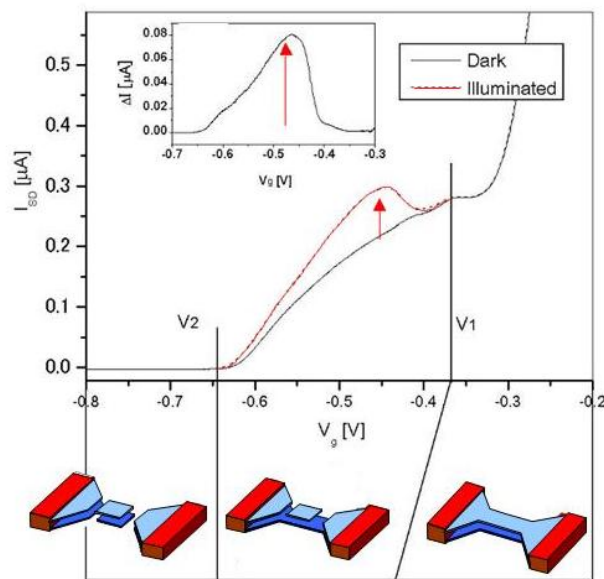
Figure 1. (a) Crystal structure for CSIP ($\lambda = 15 \mu\text{m}$). (b) The conduction-band energy diagram of DQW system. (c) Schematic representation of a CSIP as a photo-active FET.



As illustrated in Figure 1(c) the device consists of a wet-etched DQW mesa, alloyed AuGeNi ohmic contacts, Au/Ti Schottky gates, and Au/Ti photo-coupler. The device is fabricated with standard electron-beam lithography technique. Both of the QWs are connected by ohmic contacts, and can be electrically isolated by biasing metal isolation gates. The photo-coupler is used to cause intersubband transition by generating electric field normal to the plane of the QW against the normally incident radiation.

Curves in Figure 2 are the gate-bias-dependent source-drain currents with and without radiation. In dark condition the current decreases with decreasing gate bias V_g , changing the slope of its decrease at $V_g = -0.37 \text{ V}$ and completely vanishing at $V_g = -0.64 \text{ V}$. The two different slopes correspond to disconnection of each electron layer in the DQW system as schematically shown in bottom of Figure 2. Under illumination the curve increases when upper the QW is electrically isolated ($-0.64 < V_g < -0.37$).

Figure 2. I-V measurement of a CSIP with scanning gate bias V_g . Photo signal appears under illumination when floating gate is formed.



This photoresponse can be interpreted by increase of electron density in lower QW induced by capacitively coupled photoholes stored in the isolated upper QW. The unit increment of current I_e induced by one photohole in the isolated upper QW (area of $L \times W$) is given by [17,22]:

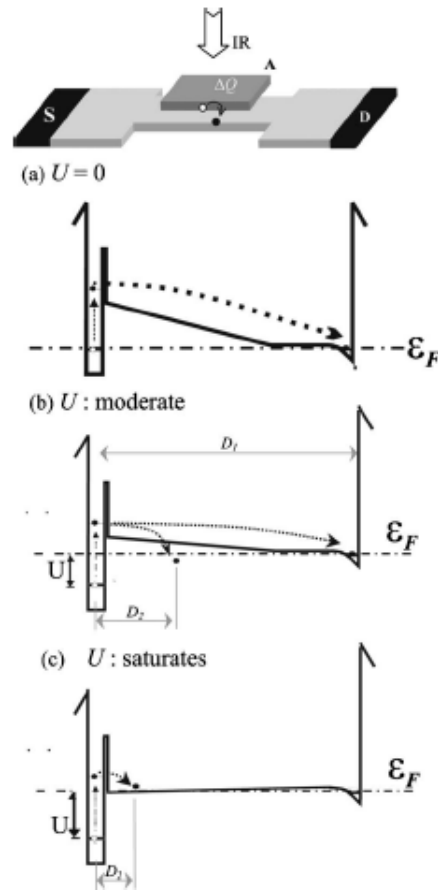
$$I_e = \frac{e\mu V_{SD}}{L^2} \quad (1)$$

where e is the unit charge, μ the electron mobility of lower QW, V_{SD} the source-drain (SD) voltage, L the length of constricted channel. For example, unit increment $I_e = 3$ pA is given for $\mu = 1$ m²/Vs, $V_{SD} = 10$ mV and $L = 16$ μm. The signal I_e persists as long as a photohole stays in upper QW. By setting the lifetime $\tau = 1$ s, the amplification factor, or photoconductive gain, is given as $G = \tau I_e / e = 1.8 \times 10^7$. This value is comparable to that of photomultiplier tubes. The increase of the current is proportional to the number of accumulated photoholes p :

$$\Delta I = p I_e \quad (2)$$

Under steady illumination, p is a linearly increasing function of time if the lifetime of photoholes is longer than the relevant time of integration. The number of photoholes, of course, does not increase infinitely, but reach a saturated value as in Figure 3. The saturation is caused by balance between generation and recombination speeds of photoholes which change with deformation of the potential profile due to accumulating positive charges in upper QW as illustrated in Figure 3 [21]. The potential drop is given by $U = pe^2 d / \epsilon L W$, where $d = 150$ nm is the distance between upper and lower QWs, $\epsilon = 12 \times (8.85 \times 10^{-12})$ F/m is the electric permittivity of GaAs.

Figure 3. Energy diagram illustrating saturation of photosignal; (a) No deformation in initial/dark condition. (b) Moderate deformation in the linear response regime. (c) Strong deformation in the saturated regime.



The number of photoholes is described by the rate equation:

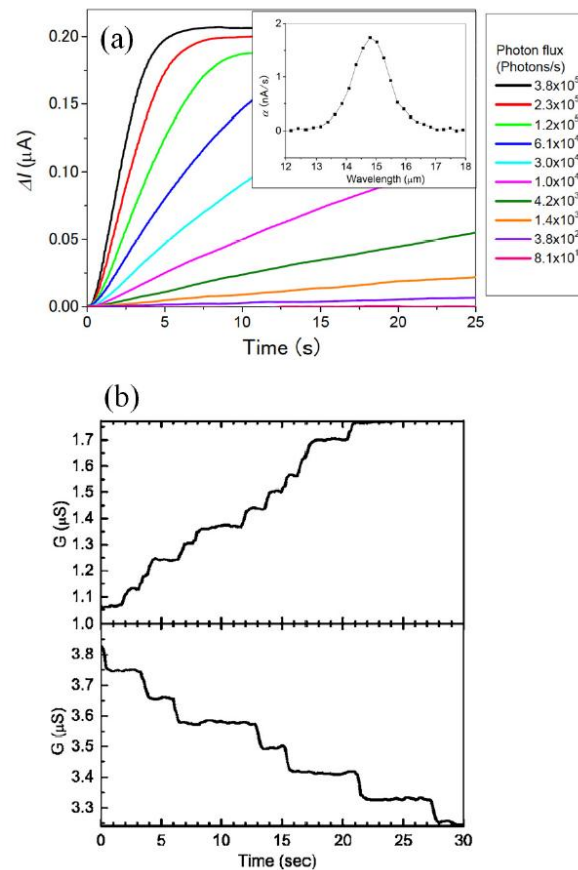
$$\frac{dp}{dt} = \eta\Phi - \frac{p}{\tau} \quad (3)$$

where η is quantum efficiency, Φ is the incident photon flux, and τ is the lifetime of photoholes. The first and second term in the right-hand side of Equation 3 refer to the generation and recombination speed of photoholes, respectively.

3. Device Operation and Photo-Signal

Figure 4 displays the photo current time traces taken at 4.2 K with a fixed surface gate bias $V_g = -0.45$ V applied at $t > 0$ s. The gate bias voltage is determined by the experiment in Figure 2. The curves in Figure 4(a) are taken with different radiation intensities. The signal curves show linearly increasing region and following saturated region. This behavior is clearly explained by Equation 3 and Figure 3: In the initial and moderate state in Figures 3(a,b), the lifetime τ is large enough to neglect second, recombination term ($p/\tau \approx 0$) and, therefore, system follows $dp/dt = \eta\Phi$. With increasing number of p , recombination term increase, and finally the system reach saturation ($dp/dt = 0$).

Figure 4. (a) Time-traces of the photo current obtained in different incident radiation intensities. The inset displays the spectrogram. (b) (Upper panel) Stepwise conductance increase seen under a weak radiation. (Lower panel) Stepwise conductance decrease seen in the dark after the measurement of the upper panel.



The signal for extremely weak radiation, which is the case of lowest photon flux in Figure 4(a), is given as stepwise increase as shown in the upper panel of Figure 4(b) [22]. The step height of $\Delta G \approx 0.05 \mu\text{S}$ is close to the value of $I_e/V_{SD} = 0.07 \mu\text{S}$ estimated from Equation 1 for active area $A = LW \approx 1.5 \times 0.8 \mu\text{m}^2$ and the mobility of lower channel $\mu \approx 1 \times 10^4 \text{ cm}^2/\text{Vs}$. This good agreement assures that each step corresponds to the single photon signal. Under dark condition, the signal then showed stepwise, slow decrease by hole-electron recombination (lower panel in Figure 4(b)). The results demonstrate extremely long lifetime of photo-generated holes (up to hours).

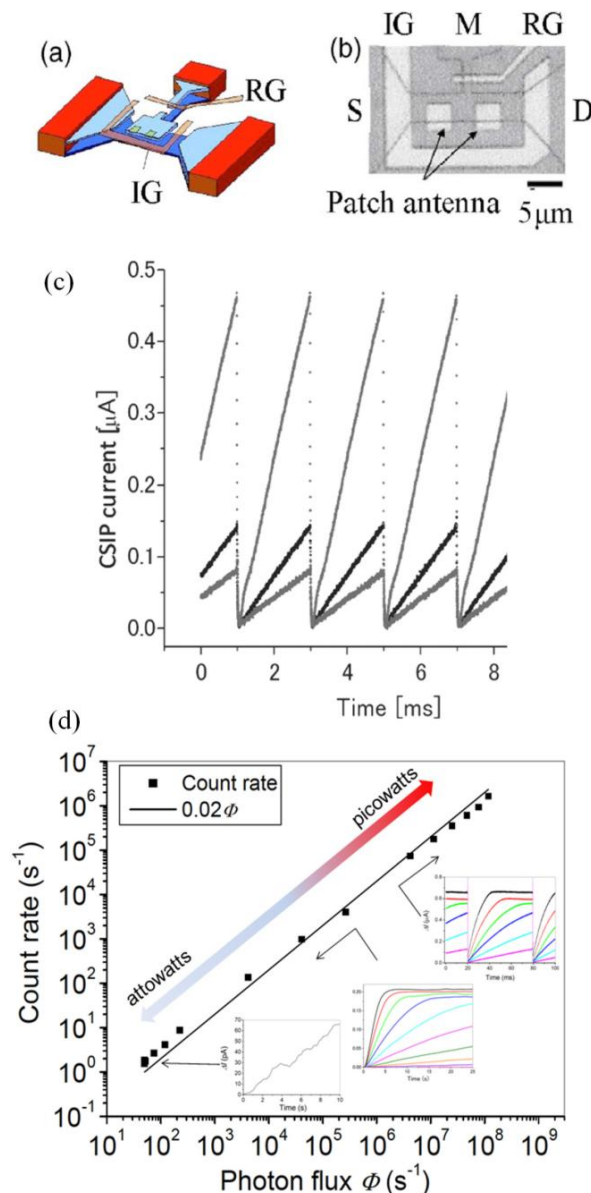
In the linear region, the photo signals of CSIPs appear as integrated single photon signals, where the slope is proportional to the photon flux via Equations 1–3: $dI/dt = I_e \eta \Phi$. However, the devices immediately reach saturation, and are no more sensitive. In practical application of CSIPs, therefore, it is very important to expand the dynamic range.

An effective method for extending the dynamic range is introducing the reset function to CSIP [23]. When a short positive pulse (1 μs -duration) is applied to an additional resetting gate (RG) in Figures 5(a,b), the accumulated charge on the isolated QW is released to the ground, and thereby resetting the device in the highly photosensitive state. The potential profile oscillates between (a) and (b) in Figure 3 by the reset operation and resulting in the linear response shown in Figure 5(c). In

Figure 5(d) we plot count rates, given by dividing linear slope dI/dt by unit signal amplitude I_e , versus photon flux $\Phi = 5 \times 10^1 - 1 \times 10^8$ tuned by the temperature of blackbody radiation source described in the next section. The original time traces are also shown in the inset of Figure 5(d). The dynamic range is extended to exceed 10^6 , where the upper limit is not given by detector but by the emitter used in the experiment [17].

Recently CSIPs for several different wavelengths are demonstrated [27,28] in 10–50 μm range (realized in 12, 15, 27, 29, 45 μm). The wavelengths are tuned by confinement of upper QW *i.e.*, width of well and height of barriers of QW. The mechanism and operation are exactly same as $\lambda = 15 \mu\text{m}$ described above.

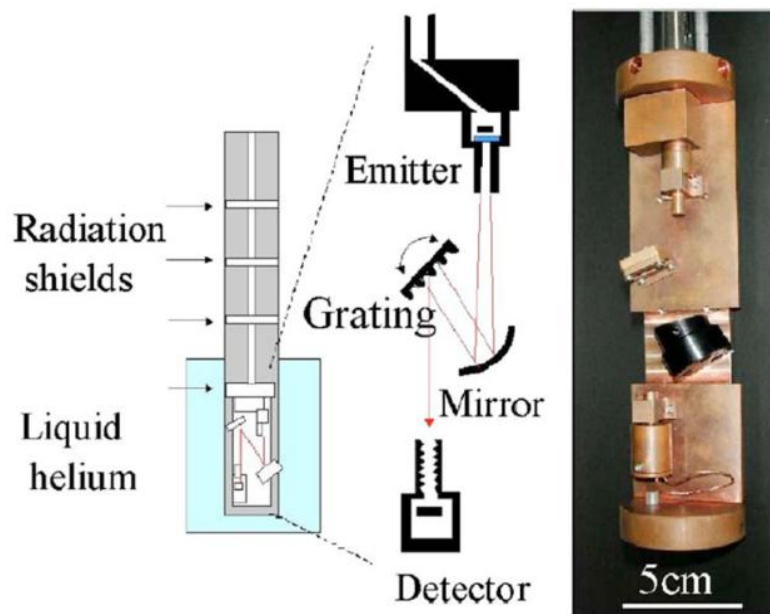
Figure 5. (a) Schematic representation of a CSIP with reset gate. IG is the isolation gate and RG is the reset gate. (b) A microscopic image of the device with $16 \times 4 \mu\text{m}^2$ isolated island formed by the upper QW. (c) Reset signal for different radiation intensities. (d) Count rate of the photo signal vs. incident photon flux Φ .



4. Figures of Merit

The quantum efficiency η , responsivity R and specific detectivity D^* of CSIP ($\lambda = 15 \mu\text{m}$) are determined accurately in all-cryogenic spectrometer [17] shown in Figure 6. In order to perform experiments without background blackbody radiation (BBR), the spectrometer is shielded by a stainless steel pipe and kept in liquid helium. The system includes glass-covered $1 \text{ k}\Omega$ thin metal chip resistor suspended in a vacuum chamber, serving as BBR source by Joule heating, and a diffraction grating to produce monochromatic photon flux. The system is necessary to accurately determine figures of merit of ultrasensitive detectors in FIR-THz range because thermal radiation from 300 K optical elements is catastrophically strong. Spectrogram and time-traces in Figure 4 (a) and Figure 5 (d) are taken by this setup. Given photon flux is accurately determined by Planck's formula with the temperature of BBR emitter monitored by a thermocouple.

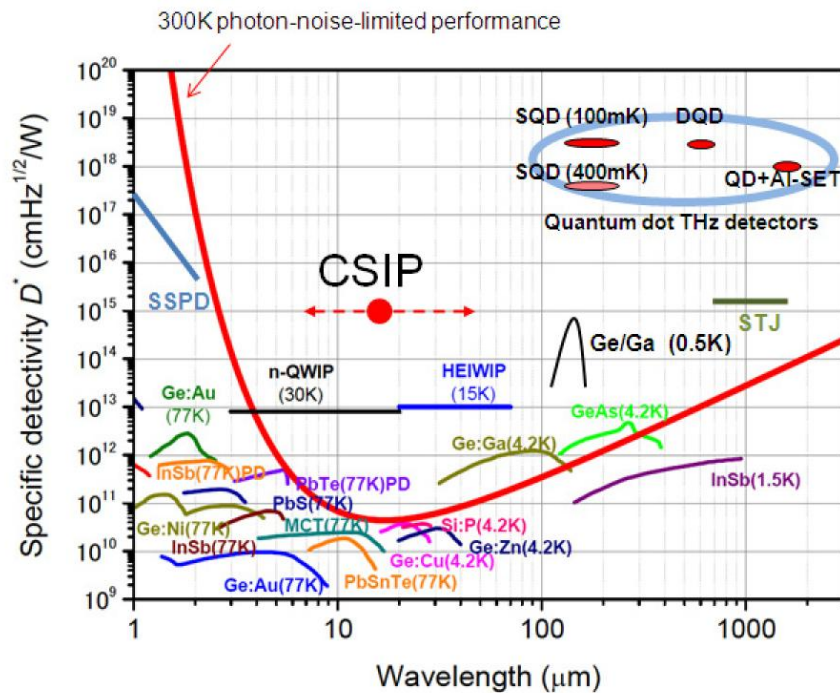
Figure 6. All-cryogenic spectrometer, schematic representation and a photograph.



The external quantum efficiency η , which includes both the coupling efficiency and absorption efficiency, directly determined to be 2% from Figure 5(d). Responsivity is the photo current amplitude divided by the incident power: $R = \Delta I/P = \eta I_e \tau_r / h\nu = 4 \times 10^4 - 4 \times 10^6 \text{ A/W}$ by noting $\eta = 0.02$, $I_e = 3 \text{ pA}$, $h\nu = 83 \text{ meV}$, and the reset interval $\tau_r = 1 \times 10^{-3}$ to 1 s.

Noise-equivalent power in photon-counting device is given as $NEP = h\nu (2\Gamma)^{1/2} / \eta$, where Γ is the dark count rate. The experimentally determined value is $NEP = 6.8 \times 10^{-19} \text{ W/Hz}^{1/2}$ from $\Gamma = 0.5$.

Specific detectivity is the reciprocal value of NEP normalized by active area A of the detector: $D^* = A^{1/2} / NEP$. With $A = 64 \times 10^{-8} \text{ cm}^2$, we have $D^* = 1.2 \times 10^{15} \text{ cm H}^{1/2}/\text{W}$. This value is compared with other conventional detectors in Figure 7. Those values are by a few orders of magnitude better than those of the state-of-the-art high-sensitivity detectors. This values even improved by improving described η in the next section.

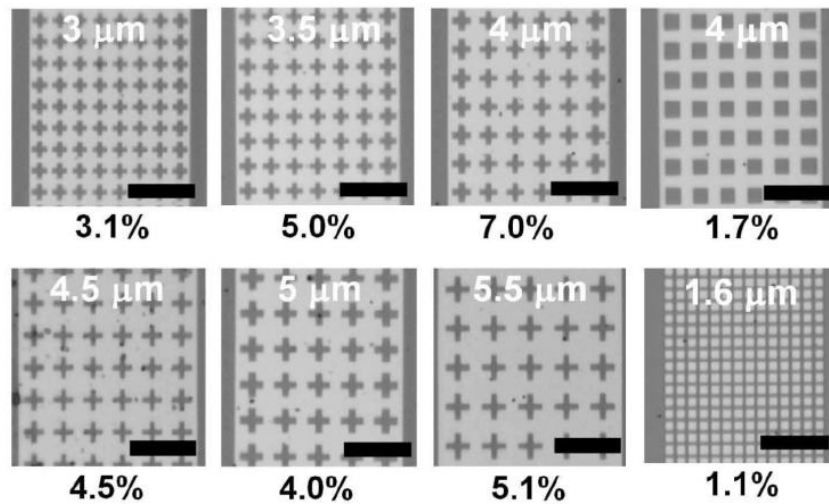
Figure 7. Spectral response characteristics of various infrared detectors.

5. Photo-Couplers for Higher Quantum Efficiency

Intersubband transition arises by electric field perpendicular to the QW plane by the selection rule. We need, therefore, photo-coupler converting direction of electric field of normal incident radiation which is parallel to the QW plane. Among excellent figures of merit of CSIPs, the quantum efficiency is limited to 2%. The relatively low efficiency arises from a low optical absorption in a single QW layer, which is in contrast with ~50% of multi-QW infrared photodetectors (QWIPs) [29].

High efficiency of QWIPs is realized by the stacked QW layers (more than 30 QWs at a depth of ~1 μm) as well as optimized photo-couplers, e.g., gratings coupled with waveguides. The photo-coupler geometries used in QWIPs, however, cannot be directly applied to CSIPs because a CSIP has only one QW for detection, which lies at a depth of 100 nm beneath the surface. Recently we proposed and demonstrated efficient photo-couplers for CSIPs ($\lambda = 15 \mu\text{m}$) by exploiting surface-plasmon-polariton (SPP) resonance occurring in aperture metal sheets coated on top of the crystal surface (Figure 8) [25]. The SPP resonance induces wavelength-selective strong electric field confined near the surface of the metal sheets, which effectively intensifies the subband transition in the QW 100 nm below the surface. Cross-shaped hole arrays yield the highest efficiency of $\eta = 7\%$, which is by a factor four higher than that of the square-metal-pad arrays. The improved quantum efficiency directly improves figures of merit described in the previous section.

Figure 8. Photo couplers. The period is marked in each micrograph. The scale bar indicates 10 μm . Numbers below each structure are the experimentally derived values of the quantum efficiency η [25].

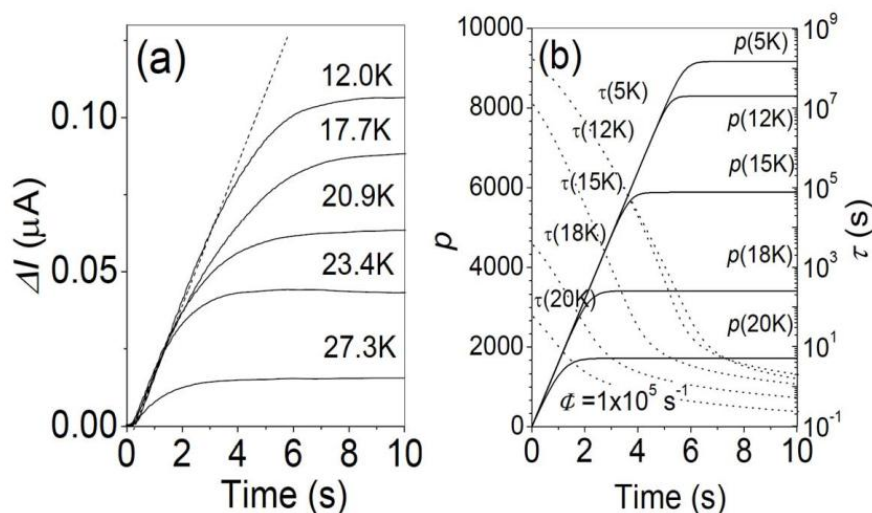


6. Temperature Dependence

Higher temperature operation is desired for practical applications. There is in general, however, a trade-off between high sensitivity and operation temperature. At the elevated temperature devices start to emit BBR or lose their sensitivity by too many thermal excited electrons overwhelming photo-excited ones.

In Figure 9(a), time traces of photo-current at different temperatures T are displayed under the fixed photon flux $\Phi = 1 \times 10^5 \text{ s}^{-1}$ [24].

Figure 9. (a) Time traces of the photocurrent with $\Phi = 1 \times 10^5 \text{ s}^{-1}$ at different temperatures. (b) Theoretical time traces of photo current in terms of p at different T (solid line), and lifetime change (dotted line) [24].



The temperature effect appears as the lower amplitude of photo-current saturation. It should be noted that the slope, $dI/dt = \eta\Phi I_e$, in the initial stage of each trace is independent of T , assuring that ηI_e is independent of T . This means higher frequency reset operation is required, *i.e.*, the integration time is shortened, in the elevated temperatures. The photo-signal is discernible up to 30 K for the CSIP of $\lambda = 15 \mu\text{m}$. The derived NEP and D^* up to $T = 23 \text{ K}$ with integration time of 1 s are given as $NEP = 8.3 \times 10^{-19} \text{ W/Hz}^{1/2}$, and $D^* = 9.6 \times 10^{14} \text{ cm Hz}^{1/2} / \text{W}$ [24], which are not very different from the 4.2 K values given at 4.2K (Section 4, [17]).

As mentioned in Section 2, the photo-current saturation occurs when the recombination process becomes equivalent to the photohole generation process. The lower level saturation at elevated temperatures is also understood by enhanced recombination: more thermally excited electrons in the lower QW contribute to the recombination process. Finally at around $T = 30 \text{ K}$, the number of traveling electron across the barrier exceeds that of photo-emitted electrons even with no band-deformation, *i.e.*, no photohole stored in upper QW.

This phenomenon can be successfully explained by a simple model by thermionic electron emission [24] which gives an expression of recombination term p/τ in Equation 3. As shown in Figure 5(b), the predicted time traces of p (photo-signal) at different temperatures substantially reproduce experimental results. The lifetime is also estimated as in Figure 5(b). It should be noted that adjustable parameters are not involved in the calculation. The model also predicts that operable temperature limit ($T = 30 \text{ K}$ for $\lambda = 15 \mu\text{m}$) is proportional to photon energy to be detected [24].

7. Conclusions

We developed novel ultrasensitive detectors in a 10–50 μm wavelength range. To our knowledge, single-photon detection is achieved in this spectral range for the first time. The accurately determined specific detectivity for CSIPs detecting $\lambda = 15 \mu\text{m}$ is a few order magnitudes superior to those of other detectors and it persists up to 23 K. Although CSIP has only one QW layer for photo absorption, the quantum efficiency has improved up to 7% by using metal mesh photo-coupler. CSIPs are featured by not only ultra-high sensitivity, but also by versatile applicability due to higher temperature operation as well as extremely wide dynamic range. The simple planar structure is feasible for array fabrication including future monolithic integration with reading circuit.

Acknowledgements

This work is supported by the CREST project of Japan Science and Technology Agency (JST).

References

1. Tonouchi, M. Cutting-Edge Terahertz Technology. *Nat. Photonics* **2007**, *1*, 97-105.
2. Rogalski, A.; Chrzanowski, K. Infrared Devices and Techniques. *Opt. Electron. Rev.* **2002**, *10*, 111-136.
3. Siegel, P.E. Terahertz Technology. *IEEE Trans. Microwave Theory Tech.* **2002**, *50*, 910-928.
4. Nagel, M.; Först, M.; Kurtz, H.; Terahertz Biosensing Devices: Fundamentals and Technology. *J. Phys. Condens. Matter* **2006**, *18*, 601-618.

5. Nakagawa, T.; Murakami, H. Mid- and Far-Infrared Astronomy Mission SPICA. *Adv. Space Res.* **2007**, *40*, 679-683.
6. Fitzgerald, A.J.; Berry, E.; Zinovev, N.N.; Walker, G.C.; Smith, M.A.; Chamberlain, J.M. An Introduction to Medical Imaging with Coherent Terahertz Frequency Radiation. *Phys. Med. Biol.* **2002**, *47*, 67-84.
7. Piesiewicz, R.; Jacob, M.; Koch, M.; Schoebel, J.; Kürner, T. Performance Analysis of Future Multigigabit Wireless Communication Systems at THz Frequencies with Highly Directive Antennas in Realistic Indoor Environments. *IEEE J. Sel. Top. Quant. Electron.* **2008**, *14*, 421-430.
8. Kawase, K.; Ogawa, Y.; Watanabe, Y.; Inoue, H. *Opt. Express.* **2003**, *11*, 2549-2554.
9. Ikushima, K.; Yoshimura, Y.; Hasegawa, H.; Komiyama, S.; Ueda, T.; Hirakawa, K. Photon-Counting Microscopy of Terahertz Radiation. *Appl. Phys. Lett.* **2006**, *88*, 152110:1-152110:3.
10. Ikushima, K.; Sakuma, H.; Yoshimura, Y.; Komiyama, S.; Ueda, T.; Hirakawa, K. THz Imaging of Cyclotron Emission in Quantum Hall Conductors. *Phys. E* **2006**, *34*, 22-26.
11. Ikushima, K.; Komiyama, S.; Ueda, T.; Hirakawa, K.; THz-Photon Generation Due to Electrons Injected via Quantum-Hall Edge Channels. *Phys. E* **2008**, *40*, 1026-1029.
12. Ikushima, K.; Asaoka, D.; Komiyama, S.; Ueda, T.; Hirakawa, K. Manipulating Terahertz Photons on a Quantum Hall Effect Device. In *Proceedings of 18th International Conference on the Electronic Properties of Two-Dimensional Systems (EP2DS-18)*, Kobe, Japan, 20-24 July 2009.
13. Schoelkopf, R.J.; Moseley, S.H.; Stahle, C.M.; Wahlgren, P.; Delsing, P. A Concept for a Submillimeter-Wave Single-Photon Counter. *IEEE Trans. Appl. Supercond.* **1999**, *9*, 2935-2939.
14. Komiyama, S.; Astavief, O.; Antonov, V.; Kutsuwa, T.; Hirai, T. A Single-Photon Detector in the Far Infrared Range. *Nature (London)* **2000**, *403*, 405-407.
15. Astavief, O.; Komiyama, S.; Kutsuwa, T.; Antonov, V.; Kawaguchi, Y.; Hirakawa, K. Single-Photon Detector in the Microwave Range. *Appl. Phys. Lett.* **2002**, *80*, 4250-4252.
16. Hashiba, H.; Antonov, V.; Kulik, L.; Tzalenchuk, A.; Kleindschmid, P.; Giblin, S.; Komiyama, S. Isolated Quantum dot in Application to Terahertz Photon Counting. *Phys. Rev. B* **2006**, *73*, 081310:1-081310:4.
17. Ueda, T.; An, Z.; Komiyama, S.; Hirakawa, K. Charge-Sensitive Infrared Phototransistors: Characterization by an All-Cryogenic Spectrometer. *J. Appl. Phys.* **2008**, *103*, 093109:1-093109:7.
18. Day, P.K.; LeDuc, H.G.; Mazin, B.A.; Vayonakis, A.; Zmuidzinas, J. A Broadband Superconducting Detector Suitable for use in Large Arrays. *Nature* **2003**, *425*, 817-821.
19. Wei, J.; Olaya, D.; Karasik, B.S.; Pereverzev, S.V.; Sergeev, A.V.; Gershenson, M.E. Ultrasensitive Hot-Electron Nanobolometers for Terahertz Astrophysics. *Nat. Nanotechnol.* **2008**, *3*, 496-500.
20. An, Z.; Chen, J.C.; Ueda, T.; Komiyama, S.; Hirakawa, K. Infrared Phototransistor Using Capacitively Coupled Two-Dimensional Electron Gas Layers. *Appl. Phys. Lett.* **2005**, *86*, 172106:1-172106:3.
21. An, Z.; Ueda, T.; Chen, J.C.; Komiyama, S.; Hirakawa, K. A Sensitive Double-Quantum-Well Infrared Phototransistors. *J. Appl. Phys.* **2006**, *100*, 044509:1-044509:7.

22. An, Z.; Ueda, T.; Komiyama, S.; Hirakawa, K. Metastable Excited States of a Closed Quantum dot with High Sensitivity to Infrared Photons. *Phys. Rev. B* **2007**, *75*, 085417:1-085417:7.
23. An, Z.; Ueda, T.; Hirakawa, K.; Komiyama, S. Reset Operation of Quantum-Well Infrared Phototransistors. *IEEE Trans. Electron. Devices* **2007**, *54*, 1776-1780.
24. Ueda, T.; Komiyama, S.; An, Z.; Hirakawa, K. Temperature Dependence of Charge-Sensitive Infrared Phototransistors. *J. Appl. Phys.* **2009**, *105*, 064517:1-064517:8.
25. Nickels, P.; Matsuda, S.; Ueda, T.; An, Z.; Komiyama, S. Metal Hole Arrays as Resonant Photo-Coupler for Charge Sensitive Infrared Phototransistors. *IEEE J. Quantum Electron.* **2010**, *46*, 384-389.
26. Wang, Z.; Komiyama, S.; Ueda, T.; Nagai, N. A Modified Scheme of Charge-Sensitive Infrared Phototransistor. *Appl. Phys. Lett.* **2009**, *95*, 022112:1-022112:3.
27. Wang, Z.; Komiyama, S.; Ueda, T.; Patrashin, M.; Hosako, I. Charge-Sensitive Infrared Phototransistor for 45 μm Wavelength. *J. Appl. Phys.* **2010**, *107*, 094508:1-094508:4.
28. Ueda, T.; Soh, Y.; Nagai, N.; Komiyama, S.; Kubota, H. unpublished work, 2009.
29. Lindqvist, L.; Andersson, J.Y.; Paska, Z.F.; Borglind, J.; Haga, D. Efficiency of Grating Coupled AlGaAs/GaAs Quantum Well Infrared Detectors. *Appl. Phys. Lett.* **1993**, *63*, 3361.

© 2010 by the authors; licensee MDPI, Basel, Switzerland. This article is an open access article distributed under the terms and conditions of the Creative Commons Attribution license (<http://creativecommons.org/licenses/by/3.0/>).